American Mineralogist, Volume 101, pages 1996–2004, 2016

SPECIAL COLLECTION: BUILDING PLANETS: THE DYNAMICS AND GEOCHEMISTRY OF CORE FORMATION

The effects of shear deformation on planetesimal core segregation: Results from in-situ X-ray micro-tomography

Kasey A. Todd[1], Heather C. Watson[2,*], Tony Yu[3], and Yanbin Wang[3]

[1]Geology and Environmental Geosciences, Northern Illinois University, Davis Hall, Normal Road, Dekalb, Illinois 60115, U.S.A.
[2]Department of Earth and Environmental Science, Rensselaer Polytechnic Institute, Troy, New York 12180, U.S.A.
[3]Center for Advanced Radiation Sources, University of Chicago, 9700 South Cass Avenue, Argonne, Illinois 60439, U.S.A.

Abstract

It is well accepted that the Earth formed by the accretion and collision of small (10–100 km), rocky bodies called planetesimals. W-Hf isotopic evidence from meteorites suggest that the cores of many planetesimals formed within a relatively short time frame of ~3 My. While a very hot, deep magma ocean is generally thought to have been the driving mechanism for core formation in large planetary bodies, it inadequately explains differentiation and core formation in small planetesimals due to temperatures potentially being insufficient for wide-scale silicate melting to occur. In order for these planetesimals to differentiate within such a relatively short time without a magma ocean, a critical melt volume of the metallic (core-forming) phase and sufficient melt connectivity and grain size must have existed to attain the required permeability and lead to efficient core formation. Shear deformation may increase the connectedness of melt and the permeability, and thus could have been a major contributing factor in the formation of planetesimal cores. This deformation may have been caused by large impacts and collisions experienced by the planetesimals in the early solar system. The purpose of this work is to test the hypothesis that shear deformation enhances the connectivity and permeability of Fe-S melt within a solid silicate (olivine) matrix, such that rapid core formation is plausible. A rotational Drickamer apparatus (RDA) was used to heat and torsionally deform a sample of solid olivine + FeS liquid through six steps of large-strain shear deformation. After each deformation step, X-ray microtomographs were collected in the RDA to obtain in situ three-dimensional images of the sample. The resulting digital volumes were processed and permeability simulations utilizing the lattice Boltzmann method were performed to determine the effect of shear deformation on connectivity and permeability within the sample. The resulting permeabilities of the sample at various steps of deformation are the same within uncertainty and do not exhibit a change with increasing deformation. Additionally, the migration velocity calculated from the permeability of the sample is not high enough for segregation to take place within the time frame of ~3 My. In addition to further constraining the mechanism of core formation in planetesimals, the image processing techniques developed in this study will be of great benefit to future studies utilizing similar methods.

Keywords: Core formation, microtomography, permeability, lattice Boltzmann

Introduction

Core formation is a significant, yet not completely understood process in the formation of the terrestrial planets and other small, rocky bodies such as large asteroids and satellites. Hafnium-tungsten isotopic studies of the Earth's mantle and several meteorites indicate that the Earth's core likely formed in ~30–100 My after the formation of the proto-Earth, while the parent bodies of iron meteorites differentiated much faster (~1–5 My) (Kleine et al. 2002, 2009; Scherstén et al. 2006; Rubie et al. 2007; Burkhardt et al. 2008) and perhaps even before 1 My (Kruijer et al. 2014). This short timescale of 1–5 My for core formation is in agreement with the theoretical model that accretion in the early solar system took place relatively rapidly (Alexander et al. 2001; Wood et al. 2006; Rubie et al. 2007). The mechanism by which core formation took place in planetesimals largely depends upon the thermal history of the body (Rubie et al. 2007). Heat generated from ^{26}Al decay would have melted the core forming alloy in planetesimals 10–100 km in diameter (Yoshino et al. 2003; Walter and Trønnes 2004; Bizzarro et al. 2005), but may not have melted the silicate to a significant degree. In the absence of widespread silicate melting, the mechanism by which metal and silicate might have segregated in planetesimals is limited to inter-granular percolation of metallic melt through a solid silicate matrix (Yoshino et al. 2003; Watson and Roberts 2011).

In order for core formation to take place efficiently in an equilibrium setting, the metallic melt must be fully connected within the solid silicate (e.g., Roberts et al. 2007; Watson and Roberts 2011). Whether or not connectivity is achieved depends on the dihedral (wetting) angle between the liquid and solid

* Present address: Department of Physics and Astronomy, Union College, Schenectady, New York 12308, U.S.A. E-mail: watsonh@union.edu
Special collection papers can be found online at http://www.minsocam.org/MSA/AmMin/special-collections.html.

grains (von Bargen and Waff 1986). The dihedral angle (θ) can be expressed as:

$$\frac{\gamma_{ss}}{2\gamma_{sl}} = \cos\left(\frac{\theta}{2}\right)$$

where γ_{ss} and γ_{sl} refer to the solid-solid and the solid-liquid interfacial energies, respectively (Bulau et al. 1979). A dihedral angle less than 60° leads to a fully interconnected melt network in which percolation is possible even at extremely small melt volumes; while a dihedral angle greater than 60° results in isolated pockets of melt and inefficient core formation, unless a critical volume of melt is present. This critical volume of melt is known as the connectivity threshold and increases with increasing dihedral angle (von Bargen and Waff 1986).

Experiments performed at conditions relevant to the interiors of planetesimals (~1–3 GPa) have determined that for the sulfide/metal melt-solid silicate system the dihedral angle is greater than 60° (e.g., Ballhaus and Ellis 1996; Shannon and Agee 1996; Gaetani and Grove 1999; Holzheid et al. 2000; Takafuji et al. 2004; Walte et al. 2007), with an average angle of 90 ±5°. At a dihedral angle greater than 60°, the melt within planetesimals would only have percolated to the core until the pinch-off threshold was reached, below which the remaining melt would have become stranded in the solid silicate matrix (von Bargen and Waff 1986). The pinch-off threshold, determined to be between 3 and 6 vol% (Yoshino et al. 2003; Roberts et al. 2007; Watson and Roberts 2011), is slightly below the percolation threshold. Therefore, being able to quantify the critical volume of melt (percolation threshold) required to maintain percolative flow becomes essential in understanding the processes that contributed to rapid, efficient core formation in planetesimals (Watson and Roberts 2011).

Estimates of the connectivity threshold in the olivine + FeS system range from ~4 to ~17%, (Yoshino et al. 2003; Terasaki et al. 2008; Bagdassarov et al. 2009a, 2009b; Watson and Roberts 2011) with most accepted values being around 5 vol%. Although we do not have many meteorite samples of differentiated mantle materials, it is commonly thought that it is unlikely for 5 vol% of metal to remain in the mantle. If we assume that core formation efficiently removes most core material from the mantle, an alternative segregation mechanism is required to lead to efficient core formation. For conditions within planetesimals, deformation caused by large impacts, and possibly convection, have been suggested as a mechanism that may have aided in the enhanced permeability and thus the segregation of the remaining melt (Bruhn et al. 2000; Rushmer et al. 2005; Groebner and Kohlstedt 2006; Hustoft and Kohlstedt 2006). This manner of efficient core formation via deformation would preclude the necessity of widespread silicate melting (i.e., a magma ocean), particularly in smaller planetesimals that may have never reached high enough temperatures.

Experiments performed on samples of varying compositions and melt volumes indicate that shear deformation can lead to the enhanced segregation of metallic melt from a solid silicate matrix (Bruhn et al. 2000; Rushmer et al. 2005; Groebner and Kohlstedt 2006; Hustoft and Kohlstedt 2006). Deformation induced on these samples had varying outcomes, including: the enhanced interconnection of melt pockets at 4 and 7 vol% sulfide melt (Bruhn et al. 2000); the migration of melt within a solid silicate matrix (Rushmer et al. 2005; 20–25 vol%); the formation of a strong melt-preferred orientation of previously isolated melt pockets (Groebner and Kohlstedt 2006; 4 vol%); and evidence of grain boundary percolation down to a pinch-off threshold of ~1 vol% (Hustoft and Kohlstedt 2006; 3, 5, and 9 vol%). The results of these experiments support the idea that shear deformation may lead to the more efficient segregation of metallic melt from a solid silicate matrix at melt volumes close to and above 5 vol%. The main differences between this previous work and the present study include (1) some previous studies looked at melt volumes that were already significantly connected (i.e., Rushmer et al. 2005); (2) in some cases, the experiments were performed at lower pressure (300 MPa) and strain rates up to two orders of magnitude higher than those here (e.g., Groebner and Kohlstedt 2006; Hustoft and Kohlstedt 2006); and (3) the only other 3D study (Bruhn et al. 2000) is on a relatively small volume (~35 × 35 × 25 μm) that may not be fully representative of connectivity and permeability of the whole sample. Recent work by Walte et al. (2011) suggests that the behavior of metallic melt in similar systems (olivine + FeS or Au) is dominated by surface energy at low strain rates and actually may inhibit elongation of melt particles, and that melt may become concentrated into larger melt pockets.

The objective of the present study is to observe the effect of shear deformation on the permeability of an olivine + FeS sample that is close to the pinch-off threshold of ~3–6 vol% melt. Previous studies have relied upon methods, such as electrical conductivity (e.g., Yoshino et al. 2003, 2004) and using theoretical models based on 2D images of melt geometry (e.g., Hustoft and Kohlstedt 2006) that indirectly measure permeability by constraining the connection threshold. Recently, synchrotron-based X-ray micro-tomography (3D) analysis of quenched samples (Shi et al. 2013) and quenched samples coupled with numerical simulations on both the olivine-basalt system (Zhu et al. 2011; Miller et al. 2014) and the olivine Fe-S system (Watson and Roberts 2011) have demonstrated that X-ray tomography is a useful tool in determining the permeability and melt geometry in a more direct way than previous methods. Two-dimensional X-ray radiography at high pressure and temperature has been recently employed to observe the segregation process in situ (Gotou et al. 2015). Here, we combine the advantages of each of these techniques. By using in situ high-pressure X-ray microtomography (HP-XMT) coupled with numerical simulations to monitor the evolution of the same sample as it is undergoing heating and deformation, we evaluate the effect of deformation on the core segregation process.

Experimental methods

Sample synthesis and high-pressure X-ray microtomography

Starting materials consisted of optically clear San Carlos olivine crystals ($[MgO_{0.91}Fe_{0.09}]_2SiO_4$) and troilite powder (FeS). After grinding under ethanol using an agate mortar and pestle, the olivine was sieved to a grain size of 37–74 μm. Pure, powdered FeS (Alfa Aesar) was added to the dried olivine to comprise 4.5 vol% and the mixture was mixed again under ethanol further to ensure uniformity. The olivine and FeS mixture was packed into a graphite capsule and sintered in a piston-cylinder apparatus at RPI for 20 h at 1 GPa and 1250 °C. The

sample synthesis assembly is shown in Figure 1a. Previous work indicates that these conditions allow the sample to attain close to complete textural equilibrium (e.g., Gaetani and Grove 1999; Yoshino et al. 2003; Roberts et al. 2007; Watson et al. 2010). Once retrieved, the sintered sample was shaped with a diamond file into several 1 × 1 mm cylinders and prepared for high-pressure deformation and imaging experiments. Filing also served to remove the thin coating of graphite around the edge of the sintered samples.

The quenched and equilibrated sample was brought to the Advanced Photon Source (APS) at Argonne National Laboratory for in situ deformation and tomographic imaging at Sector 13 (GeoSoilEnviroCARS; GSECARS), Beamline 13-BM-D). The sample assembly used in the Drickamer cell at APS is shown in Figure 1b. The details of the experimental setup available for high-pressure X-ray tomography microscopy (HPXTM) are described by Wang et al. (2005, 2011). Due to the large X-ray absorption contrast between the olivine and FeS metal, the two materials can be easily distinguished in the resulting tomographic images at a photon energy of 37 keV (Wang et al. 2011). A major advantage of using HPXTM is that the sample can be imaged in situ at high pressure and temperature, and so the *evolution* of one sample can be recorded and observed over time.

Tomographic image collection was performed using a 4″ tube with a 5× objective lens, resulting in a pixel size of 2 μm. The exposure time was 25 s per frame. White field images were collected before and after each set of tomography images to remove artifacts. The large Si (111) Bragg-Bragg monochromator allows easy switching between monochromatic and white radiation in seconds (see Wang et al. 2011). Sample pressure was monitored by energy-dispersive X-ray diffraction of the MgO pressure standard in the sample assembly and was maintained at 10 tons (~1.5 ± 0.5 GPa) during the experiment (Speziale et al. 2001). Temperature was estimated through the use of a power curve calibrated at GSECARS for this experimental assembly. Temperatures were 1100 ± 100 °C during the deformation process and lowered to ~850 °C during tomographic image collection. Shear strain was applied to the sample by rotating the upper and lower tungsten carbide anvils at constant speed in opposite directions, each at 90° steps (Fig. 2), for a total of 180° of twist. Each step of deformation lasted for approximately 1.25 h. Using the total angular rotation (840°) and the total duration of the experiment (6.25 h), a maximum apparent shear strain rate of 7.70E-5 s^{-1} was obtained. However, this is only a rough estimate of the strain rate experienced by the outer diameter of the sample and is considered an upper bound due to slippage that occurs between the rotating anvils and the sample during torsion. This strain rate is lower than that reported by previous workers on a similar system (e.g., Groebner and Kohlstedt 2006; Hustoft and Kohlstedt 2006), where strain rates varied from 10^{-2} to 10^{-4}. Walte et al. (2011) report similar strain rates to our reported maximum (7×10^{-6} to 1×10^{-4}).

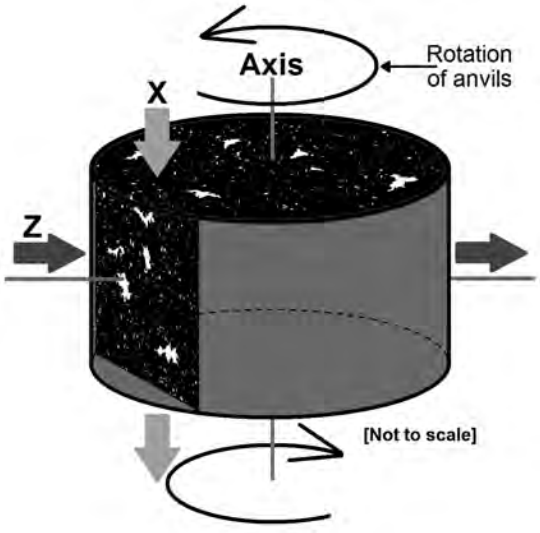

Figure 2. Schematic illustration of the sample with the two directions of flow that permeability measurements were obtained from. The X-direction of flow is parallel to the axis of rotation, while the Z-direction is perpendicular.

Electron microprobe analysis

Backscattered electron (BSE) imaging, secondary electron (SE) imaging, and wavelength-dispersive spectroscopy (WDS) were conducted on both an undeformed sample of the starting material and the deformed sample using the Cameca SX100 electron microprobe at Rensselaer Polytechnic Institute. All imaging was conducted at 15 kV, with a beam current of 50 nA. The BSE images in Figure 3 show the basic textures for the undeformed and the deformed samples. The textures of the two samples are clearly different, with FeS grains in the deformed sample being much more stretched out and appear to have migrated along olivine grain boundaries. The deformed texture can be seen in Figure 3b, where FeS is present along individual olivine grain boundaries; while in the undeformed sample, FeS occupies triple-grain junctions or grain corners as more equi-dimensional blobs (Fig. 3a). The image of the deformed sample was taken from the mid-area of the

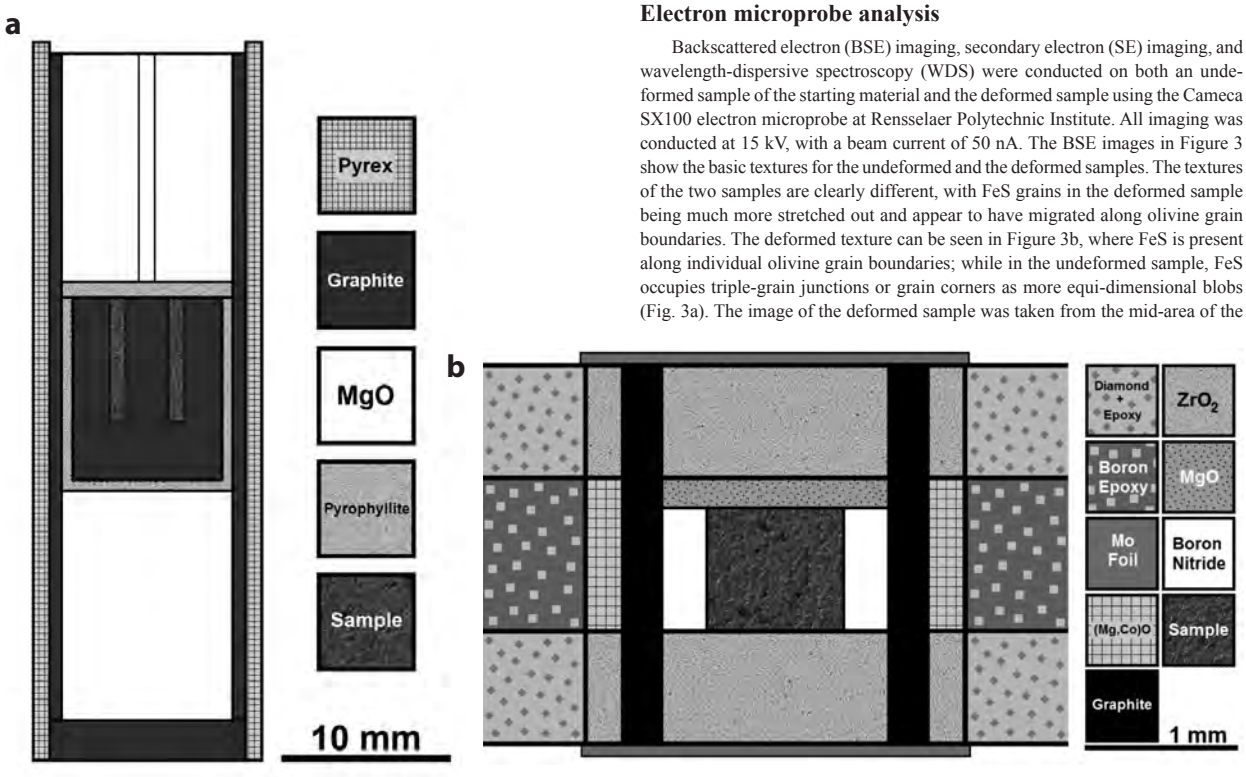

Figure 1. (**a**) Diagram of the ¾″ piston cylinder cell assembly used to synthesize the olivine + FeS starting material in a graphite capsule. (**b**) The assembly used for deformation experiments in the Drickamer cell.

sample, neither at the edge or in the center, and is broadly characteristic of the texture seen throughout the entire sample. The elongated blobs are not necessarily co-directional with the direction of shear in the sample, and are not uniformly aligned throughout the sample.

Table 1 summarizes the electron microprobe composition measurements for sulfide and olivine in both the undeformed and deformed samples. The FeS grains in the deformed sample exhibit some quench texture (sulfide immiscibility); however, this internal structure appears to have had only a slight effect on the resulting Fe and S measurements. The higher standard deviations in measurements of the deformed sample could also be attributed to the sulfide grains being thinner and more stretched out, making it more difficult to conduct measurements on a single bleb due to the beam size of a few micrometers even in spot mode. We attribute the nickel measured in the sulfide grains to an impurity in the FeS starting material. The small amount of nickel present in the olivine both before and after the deformation experiment can be attributed to the fact that nickel is occasionally substituted for iron in the crystal lattice of olivine (Kohlstedt and Mackwell 1987).

Results and discussion

Image analysis

Quantitative permeability measurements were acquired from the resulting HPXTM images. The individual radiographs collected from the beamline were reconstructed using the scientific data visualization program Tomo_Display (Rivers and Gualda 2009; http://cars9.uchicago.edu/software/idl/tomography.html) and exported as a series of TIFF images. When these individual images are stacked they create a three-dimensional volume of the sample. Six of these image stacks were chosen at increasing degrees of deformation (0°, 180°, 360°, 540°, 720°, and 840°; all at 10 tons of ram load) so that any change in permeability could be observed. Figure 4a shows a grayscale XTM image of the sample after reconstruction. These grayscale images were then binarized into regions of "melt" and "non-melt" using the program ImageJ (https://imagej.nih.gov/ij/; Fig. 4b). The appropriate threshold was determined by finding a value that would produce the correct proportion of "melt" regions given the expected value from both our synthetic starting material and initial BSE imaging of the starting material and post-deformation experiment. The melt volume percent was calculated for each image stack and found to be within one standard deviation of the starting material. The average melt fraction of the binarized XTM volumes in the X-direction is 4.36 ± 0.11% and an average of 4.44 ± 0.07% in the Z-direction, compared to the actual value of 4.5 vol%. The X- and Z-directions within the sample can be seen in Figure 2, and represent the two directions in which flow was simulated and permeability calculated. These are the two bulk directions that we can measure given the 3D data. We performed calculations in both directions because of the potential to observe anisotropy within the sample due to the shear strain applied to the sample, as well as due to potential shortening of the sample as the experiment continued. Because the nature of rotational shear results in a non-uniform strain distribution in the sample, we performed calculations of several subvolumes from different areas of the sample at each degree of deformation. There was no measurable difference in the resulting permeability in either direction, however there was a well-defined anisotropy between the two directions (see Fig. 6).

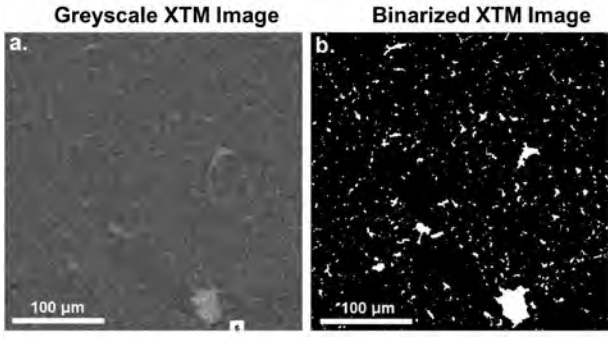

Figure 4. XTM image before and after binarization. (**a**) A gray-scale XTM image slice and (**b**) the same slice binarized. Melt is represented as the white areas, while non-melt (i.e., silicate matrix) is represented by black.

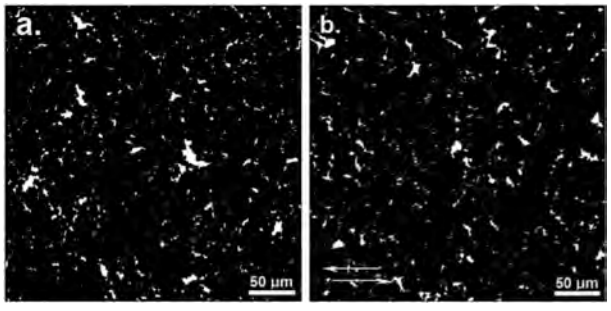

Figure 5. A binarized XTM image compared to a binarized BSE image. (**a**) Binarized XTM image of the sample deformed to 360° and (**b**) a binarized BSE image of the fully deformed sample. The texture and melt distribution in both images are very similar, indicating that the binarization process is successful in reproducing the sample texture.

Table 1. Electron microprobe results

	SiO_2	FeO	MgO	NiO	SO	Total	No. of Analyses
			Olivine (wt%)—Deformed				
Average	40.10 ± 0.28	10.55 ± 0.26	50.28 ± 0.24	0.04 ± 0.01	0.04 ± 0.03	101.02 ± 0.16	54
	Fe	S	Si	Mg	Ni	Total	No. of Analyses
			Sulfide (wt%)—Deformed				
	62.31 ± 1.45	32.01 ± 3.73	0.43 ± 0.42	0.59 ± 0.79	2.70 ± 2.36	98.04 ± 0.87	20
	SiO_2	FeO	MgO	NiO	SO	Total	No. of Analyses
			Olivine (wt%)—Undeformed				
Average	40.25 ± 0.20	10.70 ± 0.08	50.58 ± 0.09	0.05 ± 0.01	0.03 ± 0.05	101.61 ± 0.21	44
	Fe	S	Si	Mg	Ni	Total	No. of Analyses
			Sulfide (wt%)—Undeformed				
	59.21 ± 0.45	35.62 ± 0.45	0.17 ± 0.16	0.04 ± 0.04	3.54 ± 0.22	98.58 ± 0.55	21

Note: σ = one standard deviation.

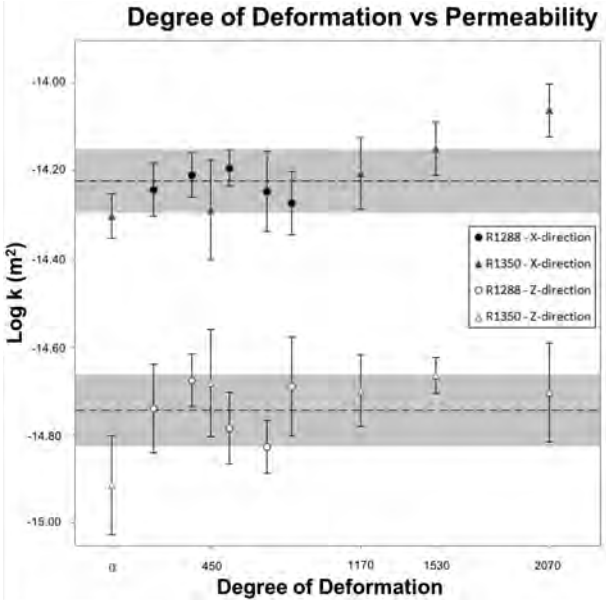

FIGURE 6. Permeability vs. degrees of deformation for two experiments. The images depicting texture in this paper are all from the first experiment (labeled R1288). The second experiment was performed in an analogous manner, but experienced significantly more deformation. The resulting final textures are very similar between both experiments, and the permeability results are consistent within uncertainty.

To approximate the true texture of the sample, the binarized XTM images were compared to the higher resolution BSE images of the deformed sample. In Figure 5, the binarized deformed sample is compared to a binarized XTM image, illustrating the similarities in texture and melt distribution between the two images. After the binarization process, the six image stacks, all with dimensions of 450 × 450 × 150 pixels, were each divided into nine 150 × 150 × 150 pixel sub-volumes and converted into digital volume input files in MATLAB.

Lattice Boltzmann simulations

The lattice Boltzmann method applied to 3D digital rock samples has been shown to be a fast and accurate method of quantifying permeability of complex geometries found in natural porous systems (e.g., White et al. 2006). Here, quantitative permeability calculations were performed on the digital volumes using the open-source program Palabos (Latt 2009), which utilizes the lattice Boltzmann method (LBM) to simulate flow of a viscous fluid through a matrix while representing the physics of a real system (Chen and Doolen 1998; Latt 2008). Palabos and the LBM have been used and validated by several previous studies (e.g., Bosl et al. 1998; Roberts et al. 2007; Degruyter et al. 2010). Palabos uses Darcy's law to obtain the permeability of the sub-volumes in non-dimensional lattice units from the average velocity distribution throughout the 3D volume, along with an applied pressure gradient and fluid viscosity. This non-dimensional value is then converted into physical units (m^2) by multiplying it with the pixel size of the XTM image.

The calculated permeabilities for various steps of shear strain for sample R1288[1] can be found in Table 2. The final measurements are all within one standard deviation of one another and do not increase with increasing deformation. Figure 6 plots the permeability results from two experiments against the steps of shear strain. The experiment labeled R1288 is the experiment shown in the images in this paper. The experiment labeled R1350 is a second experiment that was repeated using identical methods. The second experiment (R1350) was deformed to a significantly higher degree, although the final textures appeared to be similar. Also, the calculated permeabilities on both samples are consistent within uncertainty, and both samples show the sample anisotropy between the X and Z directions. This anisotropy may be a result of initial shortening of the sample due to compression at the initiation of the experiment. The one point at the highest degree of deformation in R1350 may indicate a slight shift upward in permeability at very high degrees of deformation, but more work and experiments will need to be done to confirm this result. The quantitative analysis performed on the digital volumes allows for a more direct means to calculate the permeability of the sample than previous work that relied on models such as the Kozeny-Carman relationship relating permeability to grain size and model-dependent geometric factors. The permeabilities obtained in this study are comparable to the range of values from previous workers' studies, particularly those of Roberts et al. (2007) and Watson and Roberts (2011). These studies both describe the olivine/sulfide system as well as utilize XTM images to quantitatively determine permeability via lattice Boltzmann simulations. Figure 7 compares these three studies to one another, where it can be seen that the permeabilities in this study are within one standard deviation of the permeabilities obtained for samples with higher melt fractions. It can also be seen that the results in this study have higher permeabilities than those of Watson and Roberts for the same melt fraction and the pre-deformation measurements are consistent with previous studies that state that

TABLE 2. Final permeability results for the sample R1288 in the X- and Z-directions

Angle	Melt fraction	σMF	log(k)	σlog(k)
		X-direction		
0	4.39	0.56	−14.04	0.05
180	4.53	0.89	−14.24	0.05
360	4.34	0.54	−14.21	0.04
540	4.37	0.48	−14.19	0.04
720	4.34	0.53	−14.24	0.08
840	4.20	0.61	−14.27	0.06
		Z-direction		
0	4.32	0.85	−14.52	0.08
180	4.52	1.03	−14.74	0.09
360	4.42	0.68	−14.68	0.05
540	4.45	1.00	−14.78	0.07
720	4.46	1.02	−14.83	0.05
840	4.44	0.80	−14.69	0.11

Note: σ = one standard deviation.

[1]Deposit item AM-16-95474, Video Supplemental Material. This online supplement contains four Quicktime movie (.mov) animation files that show 3D renderings of sample R1288 at different degrees of shear deformation (0, 540, 720, and 840 degrees of rotation) corresponding to a maximum strain rate of 7.7×10^{-5} s^{-1}. Each sub-volume shown has edge lengths of 485 μm on each side of the large square, and height dimensions ranging between 250 and 160 μm. The light gray particles seem in each 3D subvolume represent particles of FeS melt within the sample. The olivine component of the sample has been made transparent to allow for easier viewing of FeS blobs. Deposit items are free to all readers and found on the MSA web site, via the specific issue's Table of Contents (go to http://www.minsocam.org/MSA/AmMin/TOC/).

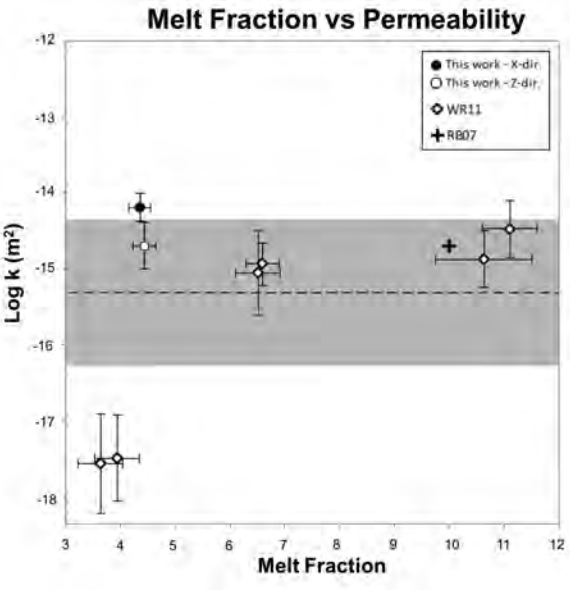

FIGURE 7. Plot of melt fraction vs. permeability comparing the results of this work to previous work. The closed circle is permeability in the X-direction for this work (4.5 vol% melt) and the open circle is for the Z-direction, with each point being an average of the full volumes in each respective direction of flow. One permeability result is shown from Roberts et al. (2007) and six results are shown from Watson and Roberts (2011). The average of the nine permeabilities is represented by the horizontal dashed lines and the gray area represents one standard deviation from this average. The sample from Roberts et al. is 10 vol%, and the results from Watson and Roberts are ~4, ~6, and ~10 vol%. The uncertainties on the data point from Roberts et al. were not available.

the pinch-off threshold in the FeS-silicate system is between 3 and 6 vol% (Yoshino et al. 2003; Roberts et al. 2007; Watson and Roberts 2011).

Comparison to previous studies

Several previous studies address the question of permeability and connectivity in similar samples with and without the complicating factor of deformation. The present work differs from these previous studies in a few important ways, as described below. In some previous work, the presence of an electrically conductive pathway has been interpreted as evidence for a melt that was sufficiently connected to allow for permeable flow (i.e., Yoshino et al. 2003, 2004). However, it has recently been shown (e.g., Watson and Roberts 2011; Watson et al. 2010) that small, disconnected, blebs of sulfide can create electrically conductive pathways. This is thought to be due to very thin (~1 nm) films along grain boundaries and edges even when the melt fraction is well below the percolation threshold (~1 vol% as opposed to 5 vol%). Because the difference in electrical conductivity is so drastic between the silicate and the sulfide melt, even a miniscule volume that is connected will produce significantly higher bulk conductivity. In these cases, the connected volume is such a small percentage of the total melt in the sample that it is unlikely to add any substantial permeability to the system. A more thorough discussion comparing estimates of permeability from electrical conductivity and X-ray micro-tomography measurements is available in Watson and Roberts (2011).

There have also been previous studies of the effect of deformation on connectivity and permeability in olivine + iron sulfide systems (e.g., Bruhn et al. 2000; Groebner and Kohlstedt 2006; Hustoft et al. 2006; Walte et al. 2011). Bruhn et al. (2000) performed experiments with a comparable volume fraction of Fe-S melt in an olivine matrix and deformed the samples at a higher strain rate of between 10^{-4} s^{-1} and 10^{-3} s^{-1} at 1250 °C and 300 MPa. In backscattered electron images they observed similar (but more pronounced) changes in the shape of the Fe-S melt blobs. The pockets became larger, more elongated, and were aligned at an angle of ~20° with the shear plane. Bruhn et al. performed a 3D reconstruction on a small portion of their sample (~35 × 35 × 25 μm) by serial sectioning and repeated BSE imaging. They interpret the changes in the melt pocket texture as evidence that melt can become interconnected and thus allow permeable flow even in systems with high dihedral angles, as a result of shear deformation. The benefit of this technique is enhanced spatial resolution of the shape of the Fe-S blob, but that comes at a cost of not being able to image as much of the sample (thousands to millions of grains and pockets), and therefore, perhaps not being able to assess the change in connectivity across the whole sample. Groebner and Kohlstedt (2006) expanded on the earlier work with more experiments on an analog system with an even higher dihedral angle of ~150° (olivine +4% Au). Again, they found a change in texture associated with deformation of the samples, and that the molten gold formed well-connected melt bands at an angle of ~15° to the shear plane. They took these results as evidence that deformation may induce more efficient percolative flow with non-wetting melts than previously believed. Again, the strain rates of these experiments were at least 2–3 orders of magnitude higher than the maximum strain rate measured here. The theory behind these results and similar results relating to the effect of shear on silicate melt extraction in the Earth is summarized in Kohlstedt and Holtzmann (2009).

Walte et al. (2011) performed a series of similar experiments on olivine + FeS, and olivine +Au across a broader range of strain rates (~10^{-4} s^{-1} to 10^{-6} s^{-1}). They analyzed the resulting textures in 2D sections of the samples, and found that the changes in textures could be categorized into different types depending on the strain rate. They show that, at high strain rates (the stress dominated regime, above ~10^{-4} s^{-1}), the samples show linear zones of elongated melt pockets, and that the degree of elongation increases with increased strain rate. At lower strain rates (the surface tension dominated regime, below ~10^{-5} s^{-1}), liquid pockets are not linearly aligned or significantly elongated. The textures seen in our experiments are consistent with an intermediate texture between what was observed for the high and low strain rate samples. This is also consistent with our measured maximum strain rate of 7.7×10^{-5} s^{-1}. The experiments of Walte et al. (2011) show that only a very small amount of melt is lost during the low strain rate experiments, indicating that there is limited connectivity of the melt within the sample. All of the experiments by Walte et al. (2011) show that at best, the melt segregation is inefficient, and at least a 2–3 vol% of the metallic melt is left behind in the sample, which is consistent with our present results.

IMPLICATIONS

The permeabilities obtained in this study can be used to calculate the migration velocity of a sulfide melt through an olivine matrix to determine if shear deformation can lead to core formation in small (100 km) planetesimals within the 1–5 My time frame. The rate of migration can be calculated using the relationship:

$$v = k\Delta\rho g / \eta$$

where k is the permeability, $\Delta\rho$ is the density difference between sulfide and olivine (2.0E+03 kg/m^3), g is the gravitational acceleration (0.1 m/s^2), and η is sulfide melt viscosity (0.01 kg/m·s), after Roberts et al. (2007) and Watson et al. (2011). Using the average of the permeabilities (X-direction; 6.31E-15 m^2), the migration velocity is calculated to be 0.4 cm/yr. A migration velocity of ~3.3 cm/yr is necessary to fully segregate a metallic melt into the core of a small planetesimal within 3 My (Watson and Roberts 2011).

However, migration velocity is highly dependent on grain size. Figure 8 shows that, for a melt volume of 4.5% and the conditions above, a grain size of approximately 230 μm is needed to reach a migration velocity of 3.3 cm/yr. These grain sizes are reasonable for small planetesimals (Watson and Roberts 2011). To obtain the migration velocities in Figure 6, the Kozeny-Carman relationship was used to calculate the permeabilities at increasing grain sizes:

$$k = (1/\mathrm{C}) \cdot d^2 \varphi^n$$

with C = 2000 (geometric constant), φ = 4.5 vol% (porosity), and n = 2, with n being a scaling exponent representing how close to the percolation threshold a system is. The actual grain sizes in this study were between 40 and 80 μm, and so these small sizes could be a contributing factor in the low permeabilities, and thus low migration velocities, observed in this sample. As mentioned above, caution needs to be applied when we are using the Kozeny-Carman relationship, as it is not uniquely determined for this system. The geometric terms chosen are roughly similar to those that have been used with some success to describe the olivine/basalt system at equilibrium, but it is unclear that these terms will apply equally well here. The main purpose of this calculation is to illustrate that the permeabilities measured in this olivine/FeS system are low compared to what is required for rapid core formation in planetesimals. It should be noted that increasing the exponent n from n = 2 to n = 3 (the value used for fully connected melt well above the percolation threshold by Faul 1997 and Bourbie and Zinszer 1985) decreases the permeability of the system even further. Furthermore, the migration velocity is also highly dependent on viscosity. The values calculated here can essentially be considered an upper bound, as they represent viscosities at the relatively high temperatures of 1300 °C, where some silicate melting would be expected. The viscosity of FeS melt at these high temperatures and pressures between 1 and 2 GPa is around 0.005 kg/m·s (Kono et al. 2015). But, LeBlanc and Secco (1996) showed that the viscosity of $Fe_{73}S_{27}$ melts increases by nearly an order of magnitude as the temperature is lowered to ~1100 °C (the conditions of these experiments, and reasonable conditions for this model of percolative core formation in the absence of silicate melt). Studies that obtain permeability indirectly through methods such as electrical conductivity yield migration velocities that differ by several orders of magnitude from this study and others that use HPXTM. From their electrical conductivity experiments, Yoshino et al. (2003) estimate a migration velocity of ~1–100 m/yr. This significantly higher value may be attributed to thin layers of sulfide melt between olivine grains that were unable to be imaged via XTM due to the in situ nature of the experiment and thus the decreased resolution. However, overall, the possible contribution that these narrow connections may have to the calculated permeability is likely insignificant (Roberts et al. 2007; Watson and Roberts 2011). Instead, this great difference likely stems from the fact that a direct measurement of permeability was not possible and so the Kozeny-Carman relationship was relied upon to infer permeability. In this study, the permeability was directly measured, thus the migration velocity calculated likely represents a more realistic scenario for core formation.

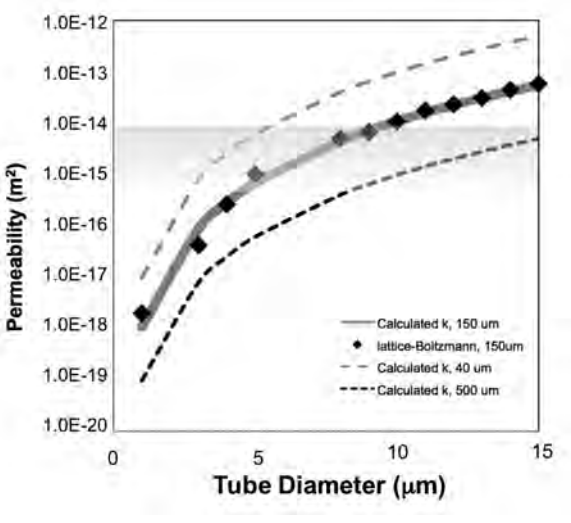

FIGURE 8. Migration velocity plotted as a function of grain size at a melt volume of 4.5%. The vertical gray dashed line represents the minimum grain size necessary (~230 μm) to attain the minimum migration velocity needed (3.3 cm/yr) in order for a small (100 km) planetesimal to fully differentiate within 3 My.

The main perceived drawback to the tomography method presented here is that the spatial resolution of the imaging is not able to capture the smallest threads of melt that could potentially be connected and create high-permeability pathways. Given our measured voxel size, we estimate that we can reliably image a feature about 2–4 μm in diameter, especially considering the large contrast between the two phases in our tomographic reconstructions. First, we note that the sulfide melt that is contributing to the permeability of the sample is a small fraction of the total melt in the sample (i.e., most of the melt is not connected). We can calculate the expected permeability of the sample given different fractions of melt that is well connected (Fig. 9). Here the data symbols represent lattice Boltzmann simulations run on artificial (ideal) volumes with a cylindrical tubules of varying diameters

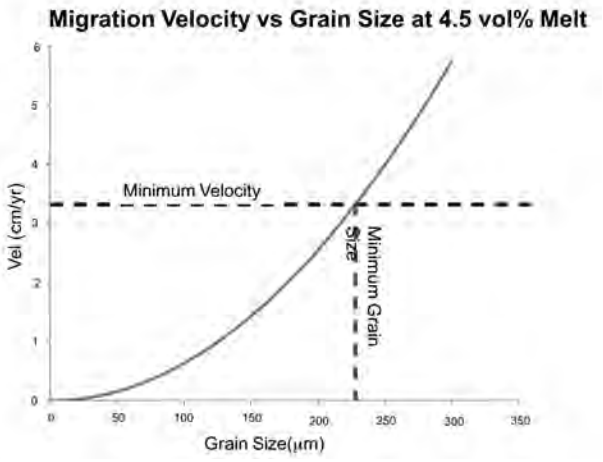

FIGURE 9. Permeability vs. tubule diameter for an idealized geometry of cubic grains of different sizes with melt tubes along grain edges. Symbols represent results from lattice Boltzmann simulations run on idealized artificial volumes, and curves are calculations of the permeability from Darcy's law for this simplified geometry.

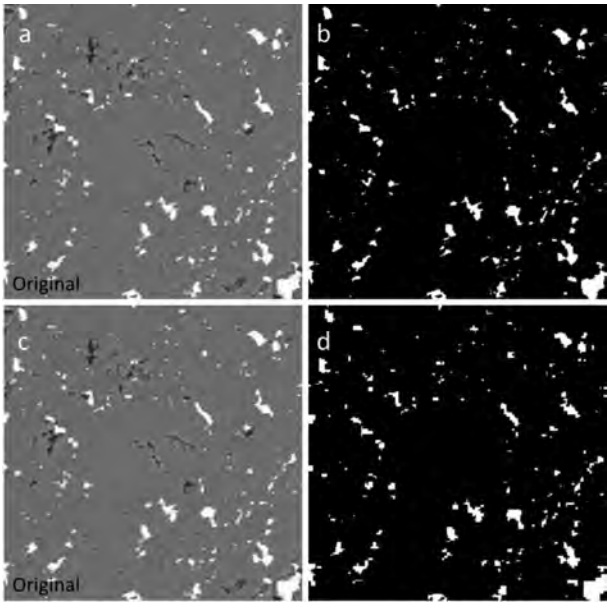

FIGURE 10. (**a**) BSE image of post-run sample. (**b**) Thresholded high-resolution BSE image. (**c**) Original BSE image again. (**d**) Thresholding of the same image that has been artificially reduced in resolution to approximate the tomography results.

along grain edges of cubic grains (150 μm edge length). The solid gray curve is the analytical solution to Darcy's law for the same geometry (Turcotte and Schubert 2002). Here we can see that our observed permeability (~10^{-15} m^2) corresponds to tubules approximately 2–3 μm in diameter. This is admittedly close to the expected resolution of what we could measure. However, to achieve an order of magnitude higher permeability, tubules of approximately 5.5 μm in diameter are predicted that we would expect to see clearly, but we do not. Second, we can compare 2D images of the sample at different spatial resolution. Figure 10 shows an example of the differences we can expect to see in thresholding a 2D backscattered electron image of the deformed sample. The first panel shows the original image, the second shows that high-resolution image thresholded directly, the fourth shows the thresholding results of an image that was artificially reduced in resolution to mimic the resolution that we would achieve by tomography (~2 μm per pixel). In both cases the images were thresholded to result in 4.6 vol% melt. Although there are some noticeable differences, the main difference tends to be around the perimeter of the larger melt blobs, which is unlikely to add significantly to the permeability. The lower resolution image does miss a few stand-alone pixels that appear in the higher resolution image, but again, these few pixels are unlikely to make a large difference in the measured permeability.

The permeabilities obtained here from the X-ray microtomographic images via lattice Boltzmann simulations indicate that the migration velocity is probably not high enough for complete core formation to take place in planetesimals within the 1–5 My time frame. However, there is still much work that can be done to increase our understanding of the effects of certain parameters such as strain rate, temperature, and metal/silicate composition on the melt connectivity, permeability, and migration velocity. These new results indicate that permeabilities obtained via XTM and the LBM are reliable and accurate; further work utilizing these methods is promising and will bring us even closer to understanding the complex and significant event of core formation in planetesimals. The development of in situ high-pressure X-ray tomography techniques allows for novel experiments to be conducted, including those that monitor the evolution of a system undergoing deformation and reaction. These new techniques greatly enhance the array of tools to investigate dynamic processes at high temperatures and pressures in more detail and with more accuracy than previously available.

ACKNOWLEDGMENTS

We thank Jared Singer for assistance with the electron microprobe at RPI, and E. Bruce Watson for use of the RPI experimental facilities to synthesize the samples. We also thank Nick Karonis and Dave Ulrick for support in using the Gaea computing cluster at NIU to perfrom lattice Boltzmann simulations. Last, we thank Nico Walte and an anonymous reviewer for comments that improved this paper. This work was supported by NSF grant GEO-1322022.

REFERENCES CITED

Alexander, C.O.D., Boss, A.P., and Carlson, R.W. (2001) The early evolution of the inner solar system: A meteoritic perspective. Science, 293(5527), 64–68.

Bagdassarov, N., Solferino, G., Golabek, G.J., and Schmidt, M.W. (2009a) Centrifuge assisted percolation of Fe–S melts in partially molten peridotite: time constraints for planetary core formation. Earth and Planetary Science Letters, 288(1), 84–95.

Bagdassarov, N., Golabek, G.J., Solferino, G., and Schmidt, M.W. (2009b) Constraints on the Fe–S melt connectivity in mantle silicates from electrical impedance measurements. Physics of the Earth and Planetary Interiors, 177, 139–146.

Ballhaus, C., and Ellis, D.J. (1996) Mobility of core melts during Earth's accretion. Earth and Planetary Science Letters, 143(1), 137–145.

Bizzarro, M., Baker, J.A., Haack, H., and Lundgaard, K.L. (2005) Rapid timescales for accretion and melting of differentiated planetesimals inferred from ^{26}Al-^{26}Mg chronometry. The Astrophysical Journal Letters, 632(1), L41.

Bosl, W.J., Dvorkin, J., and Nur, A. (1998) A study of porosity and permeability using a lattice Boltzmann simulation. Geophysical Research Letters, 25(9), 1475–1478.

Bourbie, T., and Zinszer, B. (1985) Hydraulic and acoustic properties as a function of porosity in Fontainebleau sandstone. Journal of Geophysical Research, 90(B3) 11524–11532.

Bruhn, D., Groebner, N., and Kohlstedt, D.L. (2000) An interconnected network

of core-forming melts produced by shear deformation. Nature, 403(6772), 883–886.
Bulau, J.R., Waff, H.S., and Tyburczy, J.A. (1979), Mechanical and thermodynamic constraints on fluid distribution in partial melts, Journal of Geophysical Research: Solid Earth, 84(B11), 6102–6108.
Burkhardt, C., Kleine, T., Bourdon, B., Palme, H., Zipfel, J., Friedrich, J.M., and Ebel, D.S. (2008) Hf–W mineral isochron for Ca, Al-rich inclusions: age of the solar system and the timing of core formation in planetesimals. Geochimica et Cosmochimica Acta, 72(24), 6177–6197.
Chen, S., and Doolen, G.D. (1998) Lattice Boltzmann method for fluid flows. Annual Review of Fluid Mechanics, 30(1), 329–364.
Degruyter, W., Burgisser, A., Bachmann, O., and Malaspinas, O. (2010) Synchrotron X-ray microtomography and lattice Boltzmann simulations of gas flow through volcanic pumices. Geosphere, 6(5), 470–481.
Faul, U.H. (1997) Permeability of partially molten upper mantle rocks from experiments and percolation theory. Journal of Geophysical Research, 102(B5), 10,299–10,311.
Gaetani, G.A., and Grove, T.L. (1999) Wetting of mantle olivine by sulfide melt: implications for Re/Os ratios in mantle peridotite and late-stage core formation. Earth and Planetary Science Letters, 169(1), 147–163.
Gotou, H., Yagi, T., Iizuka, R., and Suzuki, A. (2015) Application of X-ray radiography to study the segregation process of iron from silicate under high pressure and high temperature. High Pressure Research, 35(2), 130–138.
Groebner, N., and Kohlstedt, D.L. (2006) Deformation-induced metal melt networks in silicates: Implications for core–mantle interactions in planetary bodies. Earth and Planetary Science Letters, 245(3), 571–580.
Holzheid, A., Schmitz, M.D., and Grove, T.L. (2000) Textural equilibria of iron sulfide liquids in partly molten silicate aggregates and their relevance to core formation scenarios. Journal of Geophysical Research, 105(B6), 13555–13513.
Hustoft, J.W., and Kohlstedt, D.L. (2006) Metal-silicate segregation in deforming dunitic rocks. Geochemistry, Geophysics, Geosystems, 7(2), Q02001.
Kleine, T., Münker, C., Mezger, K., and Palme, H. (2002) Rapid accretion and early core formation on asteroids and the terrestrial planets from Hf–W chronometry. Nature, 418, 952–955.
Kleine, T., Touboul, M., Bourdon, B., Nimmo, F., Mezger, K., Palme, H., and Halliday, A.N. (2009) Hf–W chronology of the accretion and early evolution of asteroids and terrestrial planets. Geochimica et Cosmochimica Acta, 73(17), 5150–5188.
Kohlstedt, D.L., and Holtzmann, B.K. (2009) Shearing melt out of the earth: An experimentalist's perspective on the influence of deformation on melt extraction. Annual Reviews in Earth and Planetary Science, 37, 561–593.
Kohlstedt, D.L., and Mackwell, S.J. (1987) High-temperature stability of San Carlos olivine. Contributions to Mineralogy and Petrology, 95(2), 226–230.
Kono, Y., Kenney-Benson, C., Shibazaki, Y., Park, C., Shen, G., and Wang, Y. (2015) High-pressure viscosity of liquid Fe and FeS revisited by falling sphere viscometry using ultrafast X-ray imaging. Physics of the Earth and Planetary Interiors, 241, 57–64.
Kruijer, T.S., Touboul, M., Fischer-Gödde, M., Bermingham, K.R., Walker, R.J., and Kleine, T. (2014) Protracted core formation and rapid accretion of protoplanets. Science, 344, 1150, doi:10.1126/science.1251766.
Latt, J. (2009) Palabos, Parallel Lattice Boltzmann Solver, http://www.Palabos.com. Accessed May 2011.
LeBlanc, G.E., and Secco, R.A. (1996) Viscosity of an Fe-S liquid up to 1300 °C and 5 GPa. Geophysical Research Letters, 23(3), 213–216.
Miller, K.J., Zhu, W., Montesi, L.G.J., and Gaetani, G. (2014) Experimental quantification of permeability of partially molten mantle rock. Earth and Planetary Science Letters, 388, 273–282.
Rivers, M.L., and Gualda, G.A.R. (2009) 'tomo_display' and 'vol_tools': IDL VM packages for tomography data reconstruction, processing, and visualization, Eos Transactions of AGU, Joint Assembly Supplement.
Roberts, J.J., Kinney, J.H., Siebert, J., and Ryerson, F.J. (2007) Fe-Ni-S melt permeability in olivine: Implications for planetary core formation. Geophysical Research Letters, 34(14), doi:10.1029/2007GL030497.
Rubie, D.C., Nimmo, F., and Melosh, H.J. (2007) Formation of Earth's core. Treatise on Geophysics, 9, 51–90.
Rushmer, T., Petford, N., Humayun, M., and Campbell, A.J. (2005) Fe-liquid segregation in deforming planetesimals: Coupling core-forming compositions with transport phenomena. Earth and Planetary Science Letters, 239(3), 185–202.
Scherstén, A., Elliott, T., Hawkesworth, C., Russell, S., and Masarik, J. (2006) Hf–W evidence for rapid differentiation of iron meteorite parent bodies. Earth and Planetary Science Letters, 241(3), 530–542.
Shannon, M.C., and Agee, C.B. (1996) High pressure constraints on percolative core formation. Geophysical Research Letters, 23(20), 2717–2720.
Shi, C.Y., Zhang, L., Yang, W., Liu, Y., Wang, J., Meng, Y., Andrews, J.C., and Mao, W.L. (2013) Formation of an interconnected network of iron melt at Earth's lower mantle conditions. Nature Geoscience, 6, 971–975.
Speziale, S., Zha, C., Duffy, T.S., Hemley, R.J., and Mao, H.K. (2001) Quasi-hydrostatic compression of magnesium oxide to 52 GPa: Implications for the pressure-volume-temperature equation of state. Journal of Geophysical Research, Solid Earth, 106, B, 1, 515–528.
Takafuji, N., Hirose, K., Ono, S., Xu, F., Mitome, M., and Bando, Y. (2004) Segregation of core melts by permeable flow in the lower mantle. Earth and Planetary Science Letters, 224(3), 249–257.
Terasaki, H., Frost, D.J., Rubie, D.C., and Langenhorst, F. (2008) Percolative core formation in planetesimals. Earth and Planetary Science Letters, 273(1), 132–137.
Turcotte, D.L., and Schubert, G. (2002) Geodynamics, 2nd ed. Cambridge University Press.
von Bargen, N., and Waff, H.S. (1986) Permeabilities, interfacial areas and curvatures of partially molten systems: Results of numerical computations of equilibrium microstructures. Journal of Geophysical Research: Solid Earth (1978–2012), 91(B9), 9261–9276.
Walte, N.P., Becker, J.K., Bons, P.D., Rubie, D.C., and Frost, D.J. (2007) Liquid-distribution and attainment of textural equilibrium in a partially-molten crystalline system with a high-dihedral-angle liquid phase. Earth and Planetary Science Letters, 262(3), 517–532.
Walte, N.P., Rubie, D.C., Bons, P.D., and Frost, D.J. (2011) Deformation of a crystalline aggregate with a small percentage of high-dihedral-angle liquid: Implications for core-mantle differentiation during planetary formation. Earth and Planetary Science Letters. 305, 124–134.
Walter, M.J., and Trønnes, R.G. (2004) Early earth differentiation. Earth and Planetary Science Letters, 225(3), 253–269.
Wang, Y., Uchida, T., Westferro, F., Rivers, M.L., Nishiyama, N., Gebhardt, J., and Sutton, S.R. (2005) High-pressure X-ray tomography microscope: Synchrotron computed microtomography at high pressure and temperature. Review of Scientific Instruments, 76(7), 073709.
Wang, Y., Lesher, C., Fiquet, G., Rivers, M.L., Nishiyama, N., Siebert, J., and Guyot, F. (2011) In situ high-pressure and high-temperature X-ray microtomographic imaging during large deformation: A new technique for studying mechanical behavior of multiphase composites. Geosphere, 7(1), 40–53.
Watson, H.C., and Roberts, J.J. (2011) Connectivity of core forming melts: Experimental constraints from electrical conductivity and X-ray tomography. Physics of the Earth and Planetary Interiors, 186(3), 172–182.
Watson, H.C., Roberts, J.J., and Tyburczy, J.A. (2010) Effect of conductive impurities on electrical conductivity in polycrystalline olivine. Geophysical Research Letters, 37(2), L02302, doi:10.1029/2009GL041566.
White, J.A., Borja, R.I., and Fredrich, J.T. (2006) Calculating the effective permeability of sandstone with multi-scale lattice Boltzmann/finite element simulations. Acta Geotechnica, 1, 195–209.
Wood, B.J., Walter, M.J., and Wade, J. (2006) Accretion of the Earth and segregation of its core. Nature, 441(7095), 825–833.
Yoshino, T., Walter, M.J., and Katsura, T. (2003) Core formation in planetesimals triggered by permeable flow. Nature, 422, 154–157.
——— (2004) Connectivity of molten Fe alloy in peridotite based on in situ electrical conductivity measurements: implications for core formation in terrestrial planets. Earth and Planetary Science Letters, 222(2), 625–643.
Zhu, W., Gaetani, G., Fusseis, F., Montesi, L.G.J., and De Carlo, F. (2011) Microtomography of partially molten rocks: Three dimensional melt distribution in mantle peridotite. Science, 332, 88–91.

Manuscript received June 20, 2015
Manuscript accepted May 6, 2016
Manuscript handled by Tracy Rushmer